# Enhanced microstructure and mechanical properties of Al$_2$O$_3$-Ni composites via centrifugal slip casting with constant magnetic field

Justyna Zygmuntowicz[1]*, Magdalena Kosiorek[2,3], Marcin Wachowski[4],
Janusz Torzewski[4], I. Szachogluchowicz[4], Paulina Zielińska[5],
Waldemar Kaszuwara[1], Paweł Falkowski[6]

[1] Faculty of Materials Science and Engineering, Warsaw University of Technology, ul. Woloska 141, 02-507 Warsaw, Poland
[2] Institute of Power Engineering, National Research Institute, ul. Mory 8, 01-330 Warsaw, Poland
[3] Institute of Heat Engineering, Faculty of Power and Aeronautical Engineering, Warsaw University of Technology, ul. Nowowiejska 21/25, 00-665 Warsaw, Poland
[4] Faculty of Mechanical Engineering, Military University of Technology, ul. gen. S. Kaliskiego 2, 00-908 Warsaw, Poland
[5] Department of Materials Science, Rzeszów University of Technology, Aleja Powstańców Warszawy 12, 35-959 Rzeszow, Poland
[6] Faculty of Chemistry, Warsaw University of Technology, ul. Noakowskiego 3, 00-664 Warsaw, Poland
* Corresponding author's e-mail: justyna.zygmuntowicz@pw.edu.pl

**ABSTRACT**

This study investigates the fabrication and properties of Al$_2$O$_3$-Ni composites produced by centrifugal slip casting under a constant external magnetic field, aiming to optimize particle alignment and distribution for enhanced material performance. The research compares two series of samples made with nickel powders from Sigma Aldrich and Alfa Aesar. Series I exhibited non-uniform nickel particle distribution, while Series II demonstrated a more uniform dispersion and consistent particle size, likely due to improved alignment under the magnetic field. The optimal results from compression tests revealed that Series II achieved a compressive strength of 410 MPa, roughly twenty times greater than Series I, highlighting the effectiveness of the magnetic field in enhancing the microstructure and mechanical properties. These findings suggest that centrifugal slip casting with a constant magnetic field holds significant potential for applications in aerospace and electronics, where robust material performance under extreme conditions is required.

**Keywords:** casting, composites, mechanical properties.

## INTRODUCTION

Aluminum oxide, when reinforced with nickel particles, forms a class of ceramic-metal composites known as cermets, which possess unique properties that make them attractive to a wide range of industrial applications [1–2]. These materials combine the hardness, wear resistance, and thermal stability of ceramics with the ductility and toughness of metals, making them ideal for components subjected to extreme mechanical

and thermal stresses [3]. The specific combination of Al$_2$O$_3$ and Ni offers significant advantages in high-temperature environments, electronic applications, and aerospace technologies, where materials must endure corrosion, oxidation, and severe mechanical loads [4].

Several fabrication methods are used to produce Al$_2$O$_3$-Ni composites, each offering distinct advantages based on the desired microstructure and material properties [5–6]. Conventional powder metallurgy techniques, such as hot pressing

and sintering, are commonly employed due to their ability to achieve high-density microstructures [7–10]. However, these methods often encounter challenges in achieving a uniform distribution of metallic particles within the ceramic matrix, which is critical for consistent material performance. Additionally, they often require high sintering temperatures and extended processing times, making them energy-intensive and less suitable for large-scale production.

Other methods, such as spark plasma sintering (SPS), offer the advantages of faster sintering times and lower processing temperatures [11–13]. However, they still encounter challenges in achieving uniform distribution of the metallic phase [14–15]. Furthermore, various additive manufacturing techniques, such as direct energy deposition [16] or selective laser sintering [17], provide the capability for intricate designs. Despite these advantages, these methods require sophisticated equipment and may not consistently produce uniform microstructures [18].

Centrifugal slip casting, on the other hand, offers a significant advantage over other methods by utilizing centrifugal forces to control the distribution of the metallic phase within the ceramic matrix [19–20]. This technique involves preparing a homogeneous ceramic-metal slurry (slip) that is cast into a mold rotating at high speeds [19–20]. The centrifugal forces generated during rotation encourage the metallic particles, which typically have a higher density than the ceramic phase, to specific regions of the mold, enabling precise control over particle segregation. This technique is particularly well-suited for fabricating composite materials with graded structures or anisotropic properties.

The incorporation of an external magnetic field during the centrifugal casting process introduces an additional layer of control over the alignment and distribution of the metallic particles [21–22]. Since nickel is a ferromagnetic material, the magnetic field influences the orientation and movement of Ni particles within the $Al_2O_3$ matrix, enabling precise control of the resulting microstructure. This hybrid technique facilitates the design of composites with tailored properties, such as improved mechanical strength, thermal conductivity, or magnetic characteristics, depending on the specific alignment, distribution, and concentration of the Ni particles [21–22].

Compared to traditional methods, centrifugal slip casting with an external magnetic field offers several key advantages. First, it provides enhanced control over particle distribution, as the combination of centrifugal forces and magnetic field alignment enables a more uniform or structured dispersion of the metallic phase, a level of control that is difficult to achieve with other fabrication methods. Additionally, this process facilitates the creation of anisotropic materials, where the alignment of metallic particles imparts directional properties, making it particularly useful for applications requiring specific mechanical or thermal anisotropy. The method is also highly scalable and efficient, as it is relatively simple and cost-effective, making it suitable for industrial production in contrast to additive manufacturing techniques or highly specialized sintering processes. Furthermore, centrifugal slip casting enables the customization of composite gradients, allowing for the fabrication of functionally graded materials (FGMs). These materials exhibit variations in composition and properties across the component, enhancing performance in applications where different regions are exposed to varying loads or thermal conditions. Despite the growing technological interest in $Al_2O_3$-Ni composites, there is a relative scarcity of research on producing these materials using centrifugal casting in combination with external magnetic fields. The limited studies in this area have left a gap in understanding the influence of magnetic fields on particle distribution and the resultant material properties. Investigating these effects is essential, as they could open new avenues for enhancing the performance of ceramic-metal composites in demanding industrial applications.

This study fills an important gap in the fabrication of $Al_2O_3$-Ni composites by exploring the combined effects of centrifugal slip casting and an external constant magnetic field on the material's microstructure and properties. While prior research has investigated the individual effects of centrifugal casting and magnetic fields, their combined influence on the alignment and distribution of nickel particles – and how this impacts the composite's mechanical properties – remains underexplored. The novelty of this work lies in demonstrating how the integration of these two techniques allows for precise control over nickel particle alignment and dispersion within the alumina matrix, resulting in composites with improved mechanical performance and enhanced structural uniformity. Additionally, the study systematically compares two different nickel

powders (Sigma Aldrich and Alfa Aesar), offering insights into how variations in the powder characteristics influence microstructural gradation and overall material properties. Furthermore, the experiments varied the Ni content to assess how different nickel loadings affect the composite's properties, providing valuable guidance for optimizing the fabrication process and tailoring materials for specific industrial applications.

## MATERIALS AND METHODOLOGY

Ceramic powder $Al_2O_3$ (TM-DAR) and two types of nickel metal powders, sourced from Sigma Aldrich and Alfa Aesar, were utilized for the experiments. These powders differ in their average particle sizes. The nickel powder from Sigma Aldrich has an average particle size of 12.2 μm, whereas the nickel powder from Alfa Aesar is characterized by an average particle size of 4.8 μm. The particle size distribution for Sigma Aldrich nickel ranges from 3.8 μm to 136.5 μm, whereas the particle size for Alfa Aesar nickel ranges from 3.8 μm to 155.2 μm. To evaluate the properties of the powders, we conducted a series of characterization tests, including microscopic observations and magnetic property analyses.

The choice of deflocculants in composite preparation is crucial for achieving a stable, homogenous suspension, which directly affects the final microstructure and properties of the material. In the experiment, 0.3 wt% diammonium hydrocitrate (DAC, puriss, POCh, Poland) and 0.1 wt% citric acid (CA, ≥ 99.5%, Sigma-Aldrich, Poland) were employed as deflocculants. Both DAC and CA are known for their ability to modify the surface charge of ceramic and metal particles, such as $Al_2O_3$ and Ni, by adsorbing them onto their surfaces. This adsorption increases the zeta potential, enhancing electrostatic repulsion and preventing particle aggregation, which is crucial for achieving a stable slip. In connection with these deflocculants, the pH of the suspension should be adjusted to a range where $Al_2O_3$ particles exhibit strong repulsion due to their surface charge. Maintaining this optimal pH ensures that the slip remains fluid and homogeneous during the centrifugal slip casting process. Moreover, nickel particles, being metallic and denser, have a higher tendency to settle during casting. The use of DAC and CA minimizes this issue by ensuring even particle dispersion throughout the suspension. Previous studies and laboratory experiments have demonstrated the effectiveness of these deflocculants in ceramic-metal systems. Their use is well-established for achieving stable slurries with consistent microstructural properties, particularly in systems involving alumina and transition metals like nickel [23–25]. The small quantities (0.3 wt% DAC and 0.1 wt% CA) used are sufficient to stabilize the slip without introducing significant impurities or altering the properties of the composite, a crucial factor for ensuring high-performance applications. The dispersant-to-coagulant agent (DAC/CA) ratio played a critical role in determining the quality of nickel (Ni) particle alignment during centrifugal slip casting under a constant magnetic field. An optimized DAC/CA ratio ensured sufficient electrostatic and steric stabilization of the suspension, minimizing agglomeration and allowing Ni particles to remain individually dispersed and mobile. This mobility was essential for the particles to respond effectively to the external magnetic field and align along its direction.

The samples were fabricated using the centrifugal slip casting (CSC) method, with the incorporation of an external constant magnetic field to orient the metallic particles within the composites. The production process was divided into several stages, as illustrated in Figure 1. The diagram shows a circular arrangement of magnets surrounding the gypsum mold, with alternating N-S poles facing radially inward (Figure 1). This configuration generates a radially oriented magnetic field pointing inward toward the axis of the mold from all directions. As a result, the field lines are directed from the outer circumference of the mold toward the central axis, influencing particle alignment in the radial direction. The alternating arrangement of N and S poles around the mold suggests the field is not perfectly uniform, but instead creates a periodic radial field pattern. Such a configuration can result in a non-uniform magnetic intensity along the radial direction, with higher field gradients between the N and S poles. However, this type of setup is often used to generate sufficient magnetic torque to align ferromagnetic particles circumferentially or radially. The initial step involved accurately weighing the requisite amounts of each component. In addition to water, ceramic, and metal powders, fluidizing agents such as citric acid and diammonium hydrogen citrate were introduced to enhance interparticle interactions. These agents played a crucial role in maintaining the

stability of the suspension over time, effectively preventing sedimentation. The prepared mixtures underwent homogenization using a THINKY ARE-250 homogenizer, with ceramic balls added to the container to ensure thorough mixing throughout the staged homogenization process.

Following homogenization, the slurry was cast using a system depicted in Figure 1, which incorporates seven magnets uniformly distributed throughout the entire volume between the mold and the steel holder. In this vertical casting setup, the rotational speed was maintained at 1500 rpm for 90 minutes. Subsequent to the casting, the samples were dried and sintered in a tube furnace under a reducing atmosphere comprising 20% $H_2$ and 80% $N_2$ to inhibit the formation of spinel. The sintering process was conducted in multiple stages: the furnace temperature was first increased at a rate of 5 °C/min to 120 °C, followed by a ramp of 1 °C/min to 750 °C, and finally, at 2 °C/min to 1400 °C. The samples were held at 1400 °C for two hours before being allowed to cool to room temperature.

Once cooled, the samples were sectioned using a diamond disc saw. Some specimens were cut along the axis of rotation, while others were cut perpendicular to it. The resulting fragments were then embedded in resin for further analysis. The final stage of preparation involved grinding the samples with an automatic grinding-polishing machine (Saphir 550). This process utilized a series of discs with varying grit sizes: PLATINUM 0 (grit 80–100), PLATINUM 1 (grit 120–180),

PLATINUM 2 (grit 220–320), PLATINUM 3 (grit 600), and PLATINUM 4 (grit 1200). Two series of samples were produced, differentiated by the source of nickel powder: Series I contained Ni powder from Sigma Aldrich, while Series II utilized Ni powder from Alfa Aesar. Each series comprised 50% by volume of the solid phase, including 10% of the metallic phase.

A detailed analysis of the magnetic properties of the nickel (Ni) powders was conducted using measurements obtained with the Lakeshore VSM 7400 Vibrating Sample Magnetometer. The research investigated various magnetic parameters, including saturation magnetization, coercivity, and remanence. The primary objective was to understand the magnetic behavior of the Ni powders, which play a crucial role in applications involving the fabrication of ceramic-metal composites.

Additionally, the density, water absorption, and open porosity of the produced shapes were determined using the Archimedes method.

The raw powders and samples were observed using a JEOL JSM-6610 scanning electron microscope (SEM). Prior to observations, the samples were prepared to ensure optimal surface quality and conductivity for SEM analysis. Composite samples were mounted on aluminum stubs using conductive carbon tape to prevent charging during SEM observation. To further reduce charging effects and improve imaging quality, a thin layer of carbon (approximately $10^{-15}$ nm) was sputter-coated onto the samples using a sputter coater. The accelerating voltage was
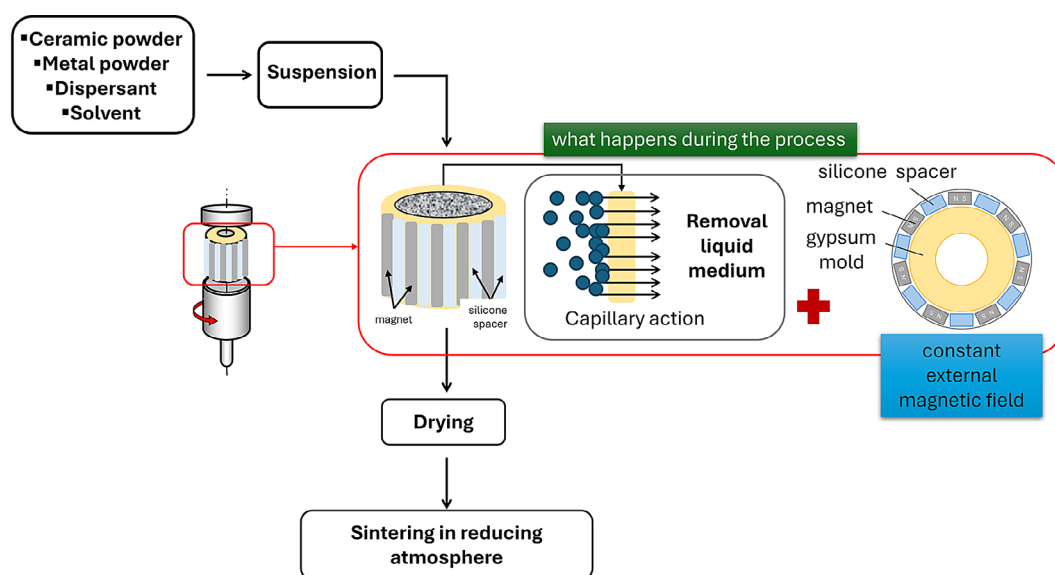


**Figure 1.** Schematic diagram of the system used to form samples using the centrifugal slip casting method using a constant magnetic field

15 kV, enabling detailed imaging of sample surfaces. The chamber pressure was maintained under high vacuum conditions (~$10^{-4}$ Pa) to ensure optimal imaging conditions for high-resolution data capture. Various magnifications were employed, depending on the level of detail required for the study. In the study, a working distance of $10^{-20}$ mm was selected to balance image resolution and depth of field, with adjustments made depending on the sample morphology. A shorter working distance was applied for high-magnification images to maximize resolution. The secondary electron (SE) detector was primarily used to capture topographical details of the sample surfaces, highlighting particle morphology and surface roughness. For compositional analysis, the backscattered electron (BSE) detector was applied to distinguish between different material phases based on atomic number contrast. Additionally, a linear study of the chemical composition of the obtained composites was performed using an Energy dispersive x-ray spectroscopy (EDS) detector. The scan length for EDS line profiles was 100 μm.

In this study, the hardness of $Al_2O_3$-Ni composites was measured using the HVS-30T hardness tester (Huatec Group Corporation, Beijing, China), following precise calibration according to the manufacturer's guidelines. Each specimen's surface was carefully prepared for flatness and smoothness to ensure reliable results. A load of 49.05 N was applied for 10 seconds, creating indentations whose diagonal lengths were measured using the instrument's optical microscope. Vickers hardness (HV) was calculated using the formula: $HV = 0.1819 \cdot F/d$, where d represents the average diagonal length (in mm), and F is the applied load (in N). Measurements were taken at 12 different locations across each sample to capture variability in hardness.

The monotonic compression test was conducted using an Instron 8802 hydraulic pulsator, selected for its ability to apply precise, high-force compressive loads. The Instron 8802 was equipped with specialized software to continuously record the load in relation to the displacement of the compression plate. The testing system's configuration enabled controlled monotonic loading, simulating realistic compressive stress conditions. A digital image correlation (DIC) system was integrated into the setup to enable real-time monitoring of the deformation process. High-speed cameras, capable of recording at frequencies exceeding 100,000 Hz, were positioned around the sample to capture detailed images of the sample surface throughout the test. The DIC system processed these images to generate strain maps, allowing for real-time visualization of strain distribution and deformation progression as the load increased. Before measurements, hollow cylindrical samples were prepared with consistent dimensions and surface qualities suitable for compressive strength testing. The sample surfaces were coated with a high-contrast speckle pattern to facilitate accurate strain measurement through the DIC system, enabling precise tracking of surface deformation during loading. During the compression test, the load was applied monotonically until sample failure, with the DIC system recording the full-field strain distribution on the sample's surface. The Instron 8802 software captured the load-displacement relationship throughout the test, generating a continuous graph showing the correlation between applied force and plate displacement. The load-displacement data obtained from the Instron 8802, combined with the strain maps from the DIC system, provided insights into the mechanical response of the samples under compressive loading. The load-displacement graph illustrated the failure stages, while the DIC strain maps enabled the identification of localized strain concentrations, crack initiation, and propagation patterns. This combined approach allowed for a comprehensive evaluation of both strength properties and failure characteristics under monotonic compression.

In the last step of this study, stereological methods were used to quantitatively analyze the growth of alumina grains following the sintering process. The investigation aimed to determine the average grain size of alumina and investigate the influence of nickel particle size on alumina grain growth during sintering. Quantitative calculations were performed using the "MicroMeter" software [26–29], leveraging data obtained from scanning electron microscopy micrographs. To ensure statistical robustness, scanning electron microscopy images of fracture surfaces were randomly selected, with at least 1.500 individual grains counted for each sample series. Grain size and distribution were analyzed using binary images derived from the binarization of grayscale SEM micrographs, enabling precise measurement of grain boundaries. This comprehensive approach provided detailed insights into the microstructural evolution of the material during sintering.

## RESULTS

Figure 2 presents SEM images and EDS results of alumina powder. The left image in Figure 2 reveals large clusters of agglomerated $Al_2O_3$ particles, with sizes ranging from approximately 5 to 20 μm. The high-magnification SEM image in the center further highlights the finer structure of these agglomerates, revealing the detailed surface morphology of $Al_2O_3$ particles at the submicron scale. The EDS spectrum on the right corresponds to the area indicated by the red square. It confirms the elemental composition of the agglomerates, showing strong peaks for aluminum and oxygen, indicating the presence of $Al_2O_3$. The EDS analysis revealed a composition of 58 wt% Al and 42 wt% O, consistent with the expected stoichiometry of alumina. The minimal presence of other elements suggests that the alumina used is of high purity.

Figure 3 presents scanning electron microscopy images and energy-dispersive X-ray spectroscopy results of two different nickel powders.

Figure 3a shows clusters of irregularly shaped nickel particles. In the magnified view, the particles appear to form a convex structure with rough surfaces. The EDS spectrum indicates (Figure 3a) that the material analyzed is composed purely of nickel, with no other significant elements detected. The sharp peak around 0 keV corresponds to carbon contamination, which is common in SEM sample preparation. However, the dominant peaks at approximately 7–8 keV confirm the presence of nickel at 100 wt%.

Figure 3b reveals that nickel powder (Alfa Aesar) displays a similar clustering of nickel particles. However, they appear slightly more angular and have a denser structure compared to Sigma Aldrich powder. The overall morphology of the particles is more compact, with well-defined edges. The EDS spectrum (Figure 3b) shows results nearly identical to those of the Sigma Aldrich powder, confirming the presence of nickel at 100 wt%, with minor carbon contamination from the sample preparation process.
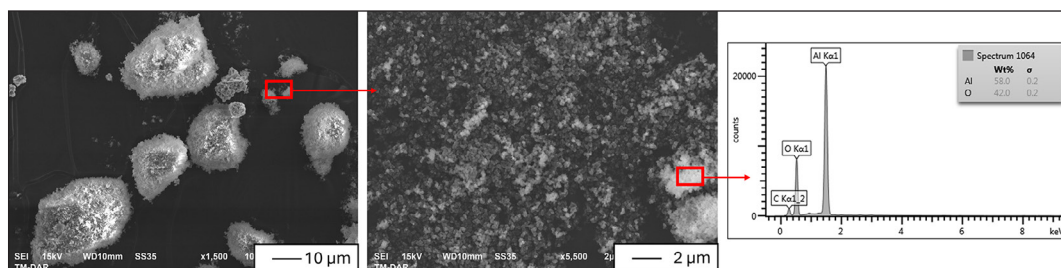


**Figure 2.** SEM micrographs and EDS spectrum of $Al_2O_3$ used in the preparation of $Al_2O_3$-Ni composites
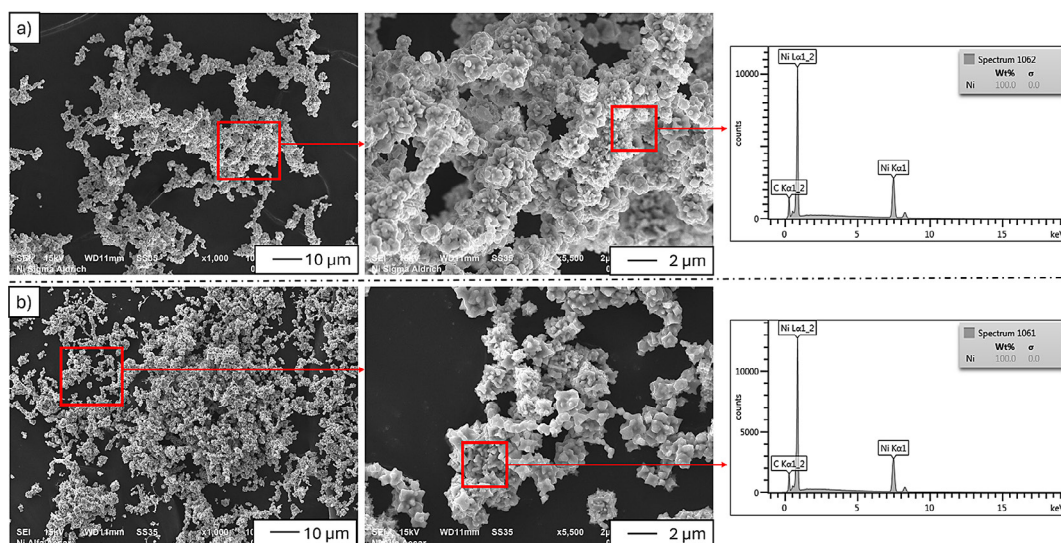


**Figure 3.** SEM images and EDS results of two different nickel powders: (a) Ni - Sigma Aldrich, (b) Ni - Alfa Aesar

In summary, both nickel powders exhibit similar elemental composition (100% Ni) but differ in their microstructural features. The Sigma Aldrich powder has a more convex shape, with numerous protuberances and rougher surfaces, while the Alfa Aesar powder appears more compact and angular. These differences in morphology could influence the distribution and interaction of nickel within composite materials.

The graphs shown in Figure 4 display the magnetic moment per mass (T) as a function of the applied magnetic field (kA/m). Key magnetic properties, including coercivity, saturation magnetization, and remanence, are highlighted. The external magnetic field required to bring the magnetic moment to zero was measured as 8.21 kA/m (102.63 Oe) for Sigma Aldrich powder and 7.66 kA/m (96.77 Oe) for Alfa Aesar powder. In the literature, such fields (referred to as coercive fields) for ferromagnetic materials can vary based on particle size, purity, and other factors [30]. The article by Crangle and Goodman on pure iron and nickel may provide comparable benchmarks for understanding the influence of particle characteristics on the coercive field [31]. The maximum magnetic moment achieved under the applied magnetic field was recorded at 0.61 T (54.589 emu/g) for Sigma Aldrich and 0.59 T (52.64 emu/g) for Alfa Aesar powder. The slight difference in magnetic moments between the two powders may indicate differences in grain structure or surface impurities, which the article discusses in the context of purity and sample preparation. The residual magnetization (remanence), measured after removing the external field, was noted as 0.08 T (6.71 emu/g) for Sigma Aldrich and 0.07 T (6.12 emu/g) for Alfa Aesar. Remanence reflects how well the material retains its magnetization after the external field is removed, an important

property in applications requiring stable magnetic characteristics without an ongoing external field [32–33]. Obtained measurements align with the typical ferromagnetic hysteresis behavior described in the literature [34], highlighting differences between the two powders, which may arise from variations in crystallographic defects or surface oxidation. The differences in magnetic properties between Sigma Aldrich and Alfa Aesar powders suggest that each may be better suited for specific applications, depending on the desired magnetic performance. Sigma Aldrich powder exhibits slightly higher values across various parameters, Potentially indicating higher purity or fewer structural defects.

Based on the Archimedes method, it was found that Series I (Ni powder from Sigma Aldrich) is characterized by an apparent density of $4.40 \pm 0.17$ g/cm$^3$, a relative density of $98.93 \pm 0.96\%$, water absorption of $0.45 \pm 0.03\%$ and open porosity of $0.85 \pm 0.11\%$. For Series II (Ni powder from Alfa Aesar), the apparent density was found to be $4.34 \pm 0.18$ g/cm$^3$. The relative density was $97.74 \pm 0.91\%$, water absorption was $0.55 \pm 0.02\%$, and open porosity was $0.96 \pm 0.08\%$. This research presents higher density and lower porosity than the previously published study [34], suggesting improved material compactness.

In the microstructures of Al$_2$O$_3$-Ni composites formed by centrifugal slip casting using a constant magnetic field, two series were examined: one with Ni Sigma Aldrich powder (Series I, Figure 5a) and one with Ni Alfa Aesar powder (Series II, Figure 5b). These two series show different nickel particle distributions across various zones. It was found that in Series I, Zone I (the leftmost area near the periphery, Figure 4a), the microstructure shows a relatively high concentration of larger, light-colored nickel particles dispersed within the
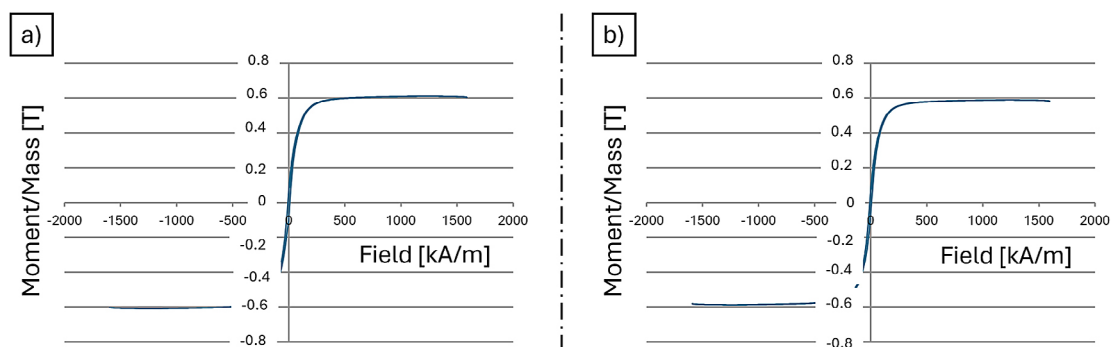


**Figure 4.** Magnetization curves of nickel (Ni) powders from two different sources: (a) Ni powder from Sigma Aldrich and (b) Ni powder from Alfa Aesar

alumina matrix. This zone appears to be denser and possibly more compact due to the effects of centrifugal casting and the capillary forces from the plaster mold. The larger nickel particles are concentrated near the periphery due to their higher density, which is influenced by the centrifugal forces during the casting process.

Further observations showed (Figure 5) that the total wall width from outer to inner edge in Series I (4.92 mm) is slightly larger than in Series II (4.69 mm). This difference may reflect variations in the slip composition or particle distribution, potentially influenced by the nickel powder's characteristics and the combined effects of centrifugal and magnetic forces. In Series I, the width of the individual zones is 8.33 mm for Zone I, 2.83 mm for Zone II, and 1.25 mm for Zone III. In contrast, for Series II, the width of the individual zones is 7.69 mm for Zone I, 3.15 mm for Zone II, and 7.69 mm for Zone III. It can be observed that Series I shows a more distinct gradient in the distribution of nickel particles, with greater variability in zone widths (Figure 5). This variability aligns with the larger particle size range and less uniform dispersion of the Sigma Aldrich powder. In contrast, Series II exhibits a more uniform distribution of nickel particles and zone widths, reflecting the finer, more consistent particle size of Alfa Aesar powder and its more uniform response to the constant magnetic field.

These findings highlight the significant impact that differences in powder characteristics and processing conditions can have on the microstructural gradation and material properties, which are essential for tailoring composite materials for specific applications.

In Zone II (Series I, middle section - Figure 5a), the particle distribution appears more uniform, but the nickel particle size is smaller and more homogeneously distributed compared to Zone I. While a slight gradient in particle density may still exist due to the casting process, the microstructure in this zone is more balanced, with a more even distribution of nickel and alumina. In Zone III (the rightmost area, closer to the center-Figure 5a), the concentration of nickel particles seems to decrease, possibly with fewer and finer nickel particles present. The alumina matrix appears to dominate in this region, suggesting that centrifugal forces had a diminished influence on particle distribution in this area.

In Series II (Figure 5b), similar observations were made for Zone I, where the periphery exhibits a dense concentration of nickel particles. However, the particles in this zone appear more uniform in size and are slightly smaller compared to those in Series I (Figure 5a). The particle distribution in this zone is evener, likely due to the finer and more consistent particle size of the Alfa Aesar powder. In Zone II of Series II (Figure 5b), the microstructure shows a more homogeneous distribution of nickel particles compared to Series I, with less variation in particle size. The observation suggests a more stable dispersion of the nickel particles during the centrifugal slip casting process. In Zone III of Series II (Figure 5b), the effects of centrifugal forces are less pronounced, similar to Zone III in Series I.

Overall, the microstructures in Series I (Figure 5a) exhibit a greater range in particle size, particularly in Zone I, where larger particles are more concentrated. In contrast, the Series II samples (Figure 5b) show a more uniform size distribution of nickel particles across the zones, suggesting a more consistent response to the centrifugal and magnetic forces during casting.
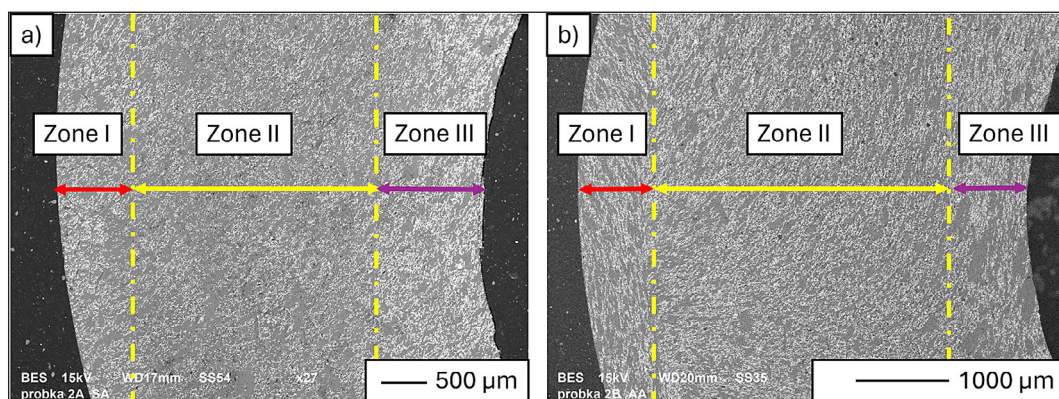


**Figure 5.** SEM images of microstructures of $Al_2O_3$-Ni composites formed by centrifugal slip casting using a constant magnetic field

Both series (Figure 5) demonstrate the characteristic effects of centrifugal casting, where heavier particles, such as nickel, migrate toward the periphery (Zone I). However, Series II (Alfa Aesar powder) shows a more uniform response to centrifugal forces. In contrast, Series I (Sigma Aldrich powder) exhibits a greater gradient in particle distribution and size across the zones. The earlier discussion primarily focused on the influence of centrifugal forces on the resulting composite structures. However, during the composite fabrication process, a constant magnetic field was simultaneously applied, significantly impacting the microstructure. Magnified views of the individual zones within the produced composites, presented in Figure 6, reveal distinct effects of the magnetic field in both Series I (Figure 6a) and Series II (Figure 6b). Notably, in Zone II of both series, the presence of relatively linear and organized patterns of nickel particles strongly suggests that the applied magnetic field influenced the microstructure. Due to their ferromagnetic nature, the nickel particles tend to align along the direction of the constant magnetic field, a behavior particularly evident in this middle zone.

The observed uniform distribution of nickel particles in Zone II, with minimal random clustering, further indicates that the constant magnetic field promoted particle alignment along specific planes during the casting process. This alignment adds an organized structure that contrasts with the distribution typically driven solely by centrifugal forces. In Zone I (the periphery), despite the dominance of centrifugal forces concentrating heavier nickel particles toward this region, the magnetic field appears to have contributed to their even distribution and organized alignment. This effect is more pronounced in Series II (Figure 6b), where nickel particles exhibit a higher degree of uniformity and organization. The interaction between the centrifugal forces and the magnetic field in this zone demonstrates that the field mitigates randomness introduced by centrifugal forces, yielding a more structured microstructure. In Zone III (closer to the center), both series show a reduction in nickel particle density due to the lower centrifugal force effect in this region. However, the particles present in this zone exhibit a degree of alignment, further implying the pervasive influence of the magnetic field across the entire sample. This alignment, even in areas with reduced particle concentration, underscores the field's role in maintaining structural organization. The observations revealed that the Alfa Aesar powder (Figure 6b) seems to respond better to the constant magnetic field compared to the Sigma Aldrich powder (Figure 6a). This distinction is most apparent in the more uniform size and alignment of nickel particles in Figure 6b. The enhanced response suggests that the morphology or composition of the Alfa Aesar powder is more compatible with the magnetic field, enabling the formation of more ordered and structured patterns within the composite.

In contrast, while the Sigma Aldrich powder (Figure 6a) exhibits magnetic field alignment, its particle distribution shows greater variability. In Zone I, the stronger influence of centrifugal forces
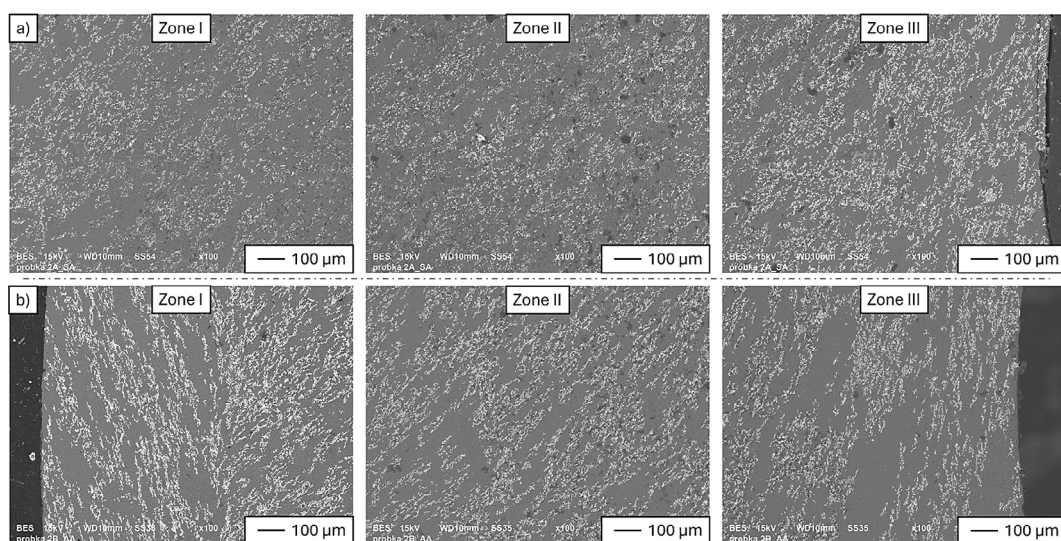


**Figure 6.** The magnifications of the individual zone areas for the $Al_2O_3$-Ni composites formed by centrifugal slip casting using a constant magnetic field

over the magnetic field on larger nickel particles is particularly evident. This results in less uniformity in particle size and arrangement compared to the Alfa Aesar sample.

By analyzing the effect of different nickel powders on the microstructure and mechanical properties of the composites, we aim to provide a more comprehensive understanding of how powder characteristics influence the final material properties. We believe that this additional dataset contributes novel insights to the field and expands the scope of our previous research [34].

Figure 7 contains two sets of data related to the elemental distribution in $Al_2O_3$-Ni composites analyzed using EDS. Observations reveal that for Series I (Sigma Aldrich Ni powder), the upper part of Figure 7a shows a micrograph of the composite material with a yellow line marking the location where the EDS line scan was performed. The lower graph in Figure 7a presents the EDS line scan results, where the X-axis represents the distance in micrometers (μm), and the Y-axis represents counts per second (cps) for the detected elements. The three plotted lines correspond to Al (green) – Aluminum from the $Al_2O_3$ matrix, O (red) – Oxygen, also primarily from the $Al_2O_3$ matrix, and Ni (cyan) – Nickel, representing the metallic phase in the composite. The fluctuating signals indicate variations in the elemental concentration across the scanned region.

For Series II (Alfa Aesar Ni powder), similar to Figure 7a, the upper part displays a micrograph (Figure 7b) of the material with a yellow line marking the EDS scan location. The lower graph (Figure 7b) shows the EDS line scan results for this series, following the same pattern as in Figure 7a. Al (green), O (red), and Ni (cyan) are detected in this scan. The variation in signals indicates the distribution of nickel particles and the alumina matrix across the scanned region.

Both figures demonstrate the elemental distribution in the composite material, with Series I and II having different microstructural characteristics. The changes in signal intensity reflect differences in the dispersion of the Ni phase within the $Al_2O_3$ matrix.

Despite the uneven distribution of nickel particles across the cross-section, the hardness test showed that the samples had a constant hardness for both series. Series I exhibited a hardness of $1731.67 \pm 11.06$ HV ($16.98 \pm 0.11$ GPa), while Series II showed a hardness of $1753.83 \pm 19.57$ HV ($17.2 \pm 0.19$ GPa). Comparing these results to previous studies that utilized the centrifugal slip casting (CSC) technique and magnetic field application [22], variations in hardness values are evident. In the previous study, hardness ranged from 970 HV to 2700 HV across different zones of the gradient composite [22]. In contrast, this research does not report zone-specific hardness. Still, highlights improved overall material
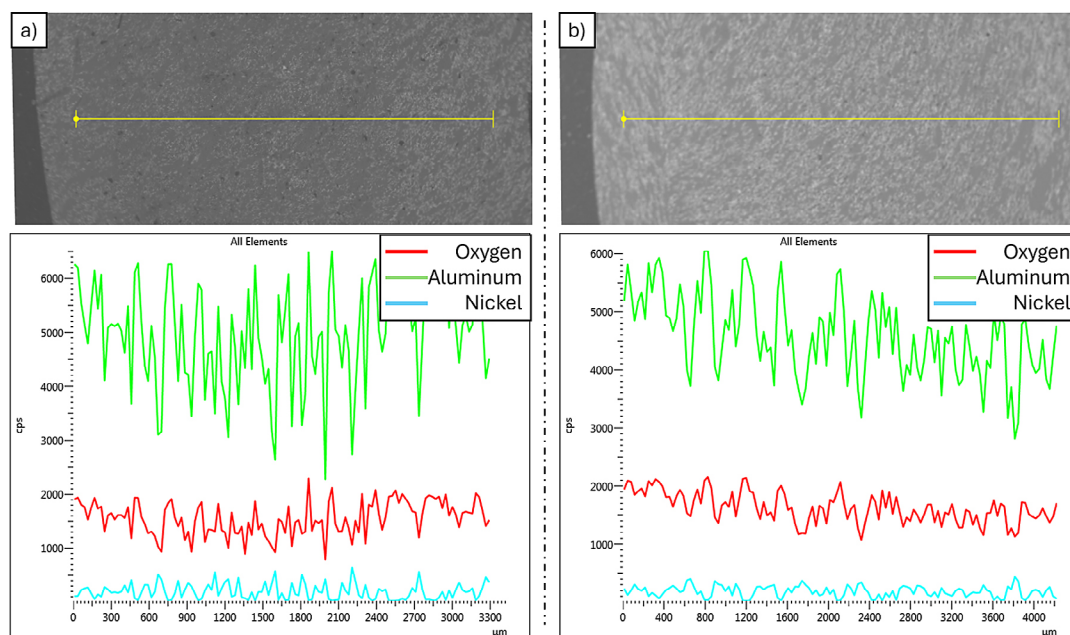


**Figure 7.** Two sets of data related to the elemental distribution in $Al_2O_3$-Ni composites were analyzed using energy-dispersive X-ray spectroscopy: (a) Series I, (b) Series II
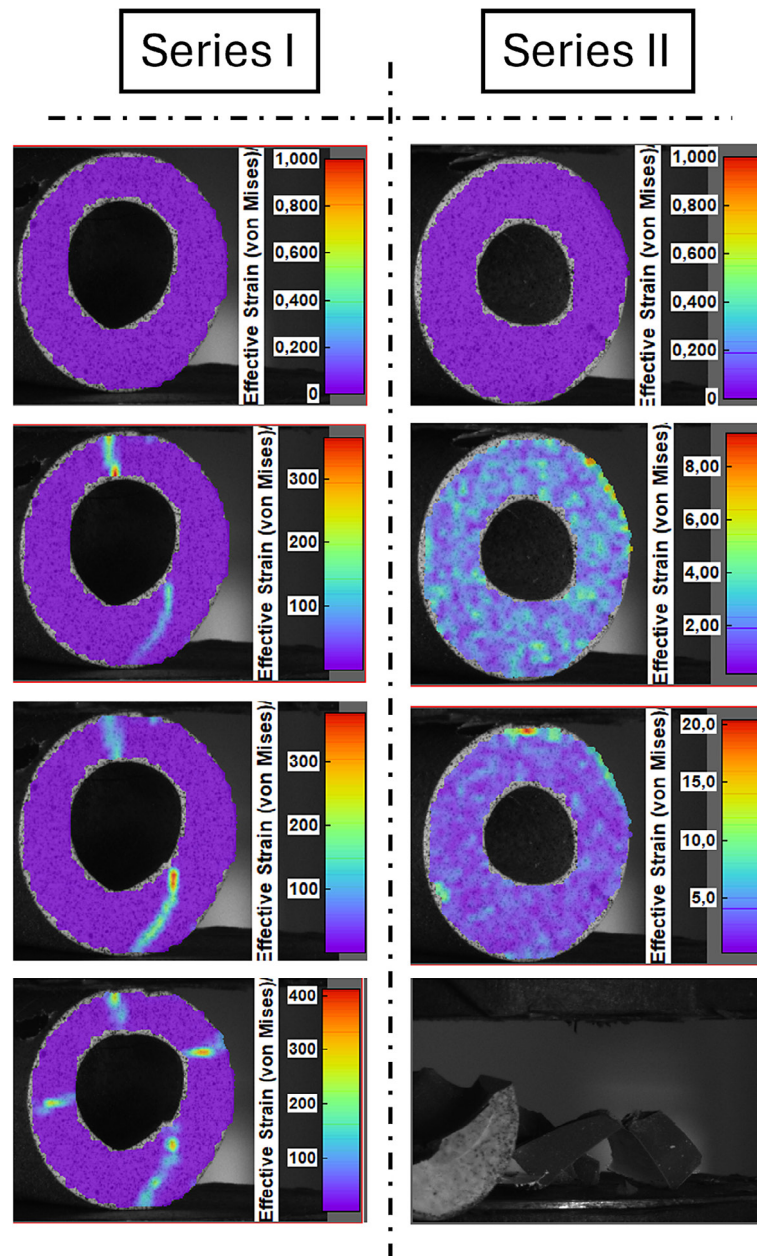
**Figure 8.** Exemplary strain distribution using the digital image correlation technique for the $Al_2O_3$-Ni composites

performance due to uniform particle distribution and better alignment through the influence of a constant magnetic field.

Compression tests revealed distinct behaviors between the two series. The Series I sample exhibited a classic cracking pattern, with cracks initiating along the vertical axis (Figure 8, left side), consistent with the location of the applied load. Notably, the primary crack initiates at the bottom of the sample and grows to the right, although theoretically, it should progress vertically upward. Lateral cracks appeared predictably, and cross cracks confirmed the material's brittleness and lower compressive strength. In contrast, the

sample from Series II demonstrated very stable behavior throughout the compression process. The range of deformations was small and uniformly distributed across the entire transverse surface of the sample. The Series I sample showed minimal deformation capacity and shattered upon exceeding the maximum compressive strength (Figure 8, right side). The uniform load transfer indicated the absence of manufacturing defects. This behavior reflects the high compressive strength and significant brittleness of the material.

Figure 9 presents the results of the monotonic compression test for the two composite samples. Analysis of the curve revealed significant

differences in compressive strengths. The sample from Series II (410 MPa) exhibited nearly twenty times the strength of the sample from Series I (21 MPa). Additionally, the specimen from Series II exhibited significantly higher ductility. Despite the differences in strength values, the stress-displacement curves for both samples showed similar trends. In the initial loading phase, a slight slope was observed, followed by a more linear progression, culminating in a sharp load drop during the final phase. This sharp decrease corresponds to crack initiation and reflects a dynamic brittle fracture, as confirmed by the DIC analysis (Figure 9). The observed linear increase in load before failure also indicates the absence of structural artifacts in the composite material. The compressive strength values obtained in this study were found to be higher than those reported in the authors' previous research. Previous studies indicated that for $Al_2O_3$/Ni composites containing 50 vol% solid phase and 10 vol% metallic phase formed by centrifugal slip casting, a compressive strength of 42.45 MPa was achieved [21]. By comparison, the Series II material in this study demonstrated strength approximately ten times greater.

When comparing the results to another previous study, which used identical starting powders but a different composite-forming system, further improvement in durability was observed. Specifically, the compressive strength of Series II composites reached 410 MPa, significantly higher than the 128.92 MPa reported in the earlier work

[22]. This enhanced performance is attributed to the optimized alignment and distribution of nickel particles within the $Al_2O_3$ matrix, achieved through the refined sample-forming technique employed in this study. These results underscore the potential of the methodology used in this research to achieve exceptional mechanical performance. The improvement in compressive strength highlights the applicability of these composites in demanding fields such as aerospace and electronics, where high material strength is critical.

It is worth paying attention to the fact that both Series I and II showed comparable hardness values (~1730–1750 HV) despite significant differences in nickel particle distribution and compressive strength, due to the nature of what hardness measures and how it responds to microstructural factors. Hardness in these composites is primarily governed by the $Al_2O_3$ matrix, which is much harder than nickel. Since nickel content was only 10 vol%, the influence of its distribution on hardness was minimal. The hardness test mainly probes the resistance to localized plastic deformation, which is dictated by the ceramic phase. Vickers hardness tests involve a very small contact area (on the order of microns). This means the indenter often interacts with a mostly ceramic region, regardless of the broader distribution of Ni particles (Figure 10 a). Unless the nickel forms a continuous or significantly clustered phase at the micro-scale indentation point, its presence does not strongly alter the result. Even where nickel particles are present near the surface, their
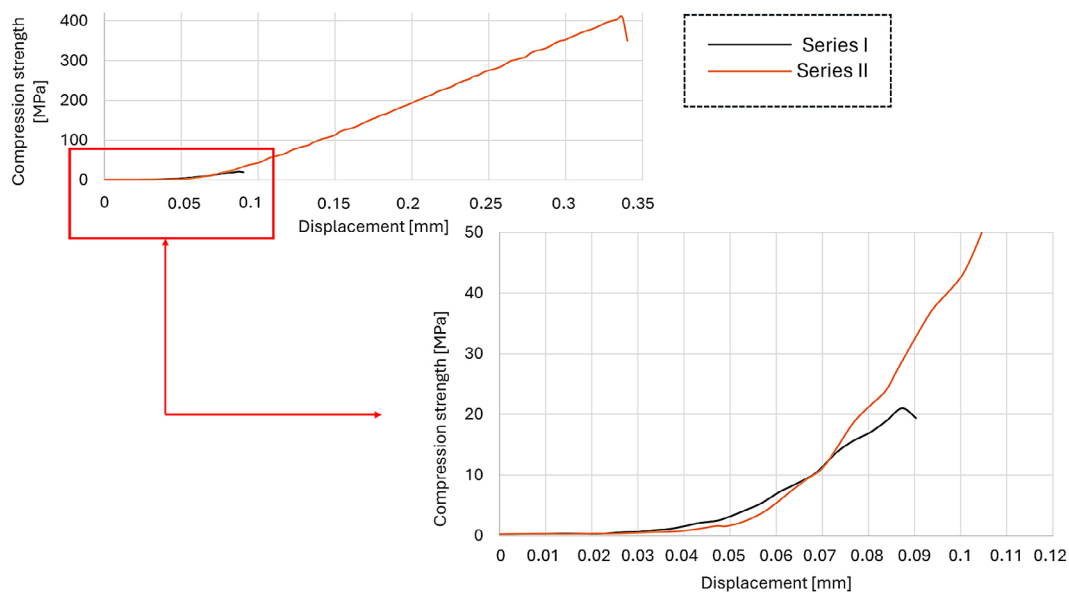


**Figure 9.** Scheme of deformation as a result of monotonic compression for the $Al_2O_3$-Ni specimens

ductile nature means they undergo limited plastic deformation under the indenter, blunting the stress but not lowering the hardness dramatically. Their isolated presence doesn't dominate the response. In contrast, compressive strength is sensitive to macro- and microstructural defects, including particle clustering, alignment, and interfacial bonding. Series I's poor particle distribution introduced stress concentrators and weak zones, drastically reducing strength, something hardness tests cannot detect (Figure 10 b). Hence, even a poorly dispersed metallic phase may not reduce hardness significantly, while it can critically impair compressive strength.

Figure 11 presents SEM images of the fracture surfaces of $Al_2O_3$–Ni composites after mechanical testing, highlighting the morphology and fracture behavior of the ceramic matrix. In both Series I and Series II, well-defined $Al_2O_3$ grains are visible, indicating that the fracture propagated through the sintered ceramic network. The fracture surfaces display features consistent with a predominantly transgranular fracture mode, characterized by cleavage-like steps and faceted grain boundaries, particularly evident in the larger grains of Series II. These features suggest strong intergranular cohesion and indicate that crack propagation occurred preferentially through grains rather than along grain boundaries. This transgranular behavior is often associated with higher mechanical strength, as more energy is required for cracks to traverse individual
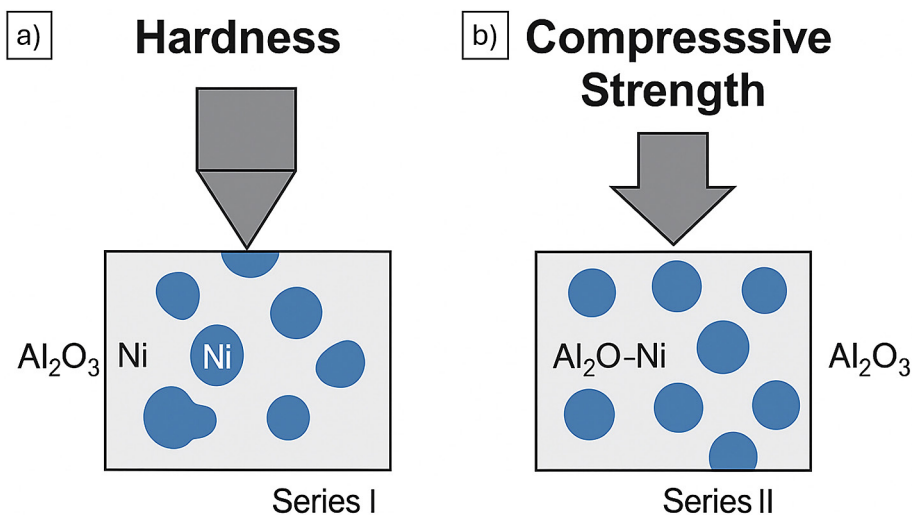


**Figure 10.** Schematic illustration comparing the effects of nickel (Ni) particle distribution on hardness and compressive strength in $Al_2O_3$-Ni composites. Despite the irregular Ni dispersion in Series I (left (a)), hardness remains high due to the dominant ceramic matrix. In contrast, the uniform Ni alignment in Series II (right (b)) significantly enhances compressive strength by improving structural integrity and load distribution
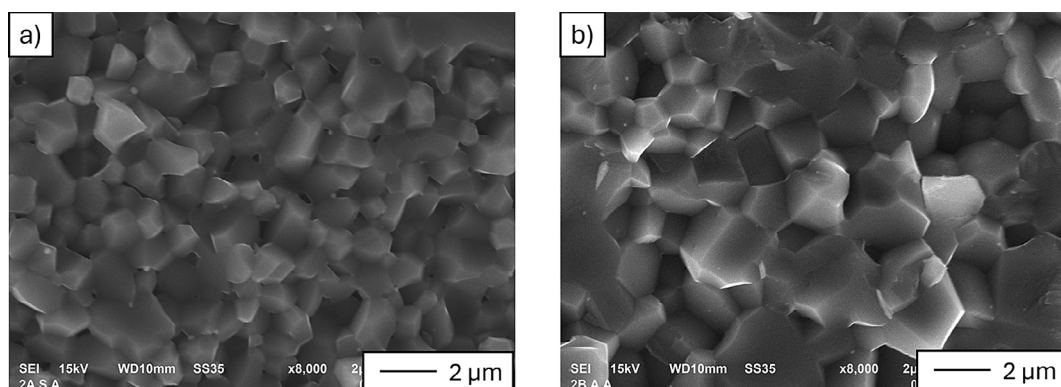


**Figure 11.** SEM images of fracture surfaces of $Al_2O_3$–Ni composites: (a) Series I and (b) Series II. The micrographs reveal predominantly transgranular fracture, with well-developed and faceted $Al_2O_3$ grains Series II shows larger, more tightly packed grains, consistent with its superior mechanical performance
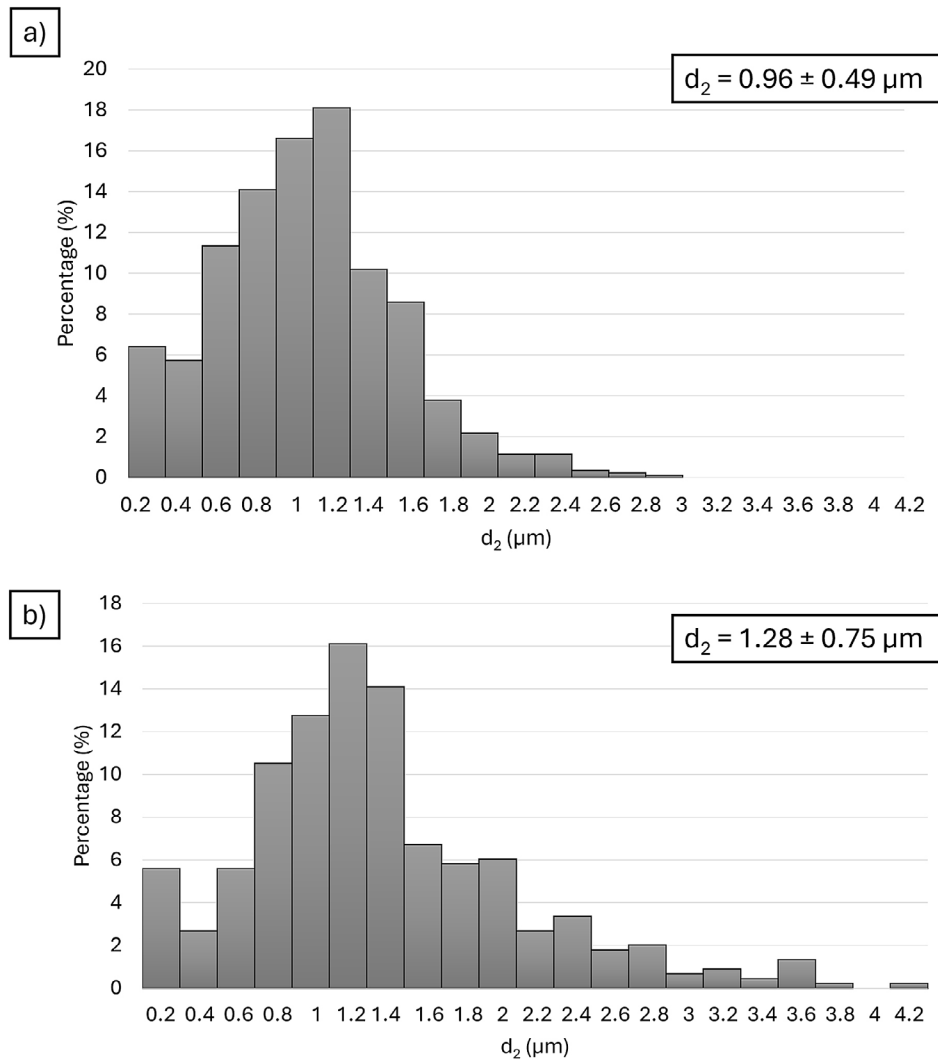
**Figure 12.** Grain size distribution of $Al_2O_3$ in $Al_2O_3$-Ni composites: (a) Series I, (b) Series II

grains. Despite the larger grain size in Series II, the microstructure appears more cohesive and densely packed, which correlates with the significantly improved compressive strength observed in these samples.

The results indicate that employing a system with seven evenly distributed magnets placed between the mold and the steel holder, combined with spinning at 1500 rpm for 90 minutes, leads to improved mechanical properties compared to classical centrifugal slip casting with a magnetic field. Figure 12 a shows the histogram that displays the grain size distribution of $Al_2O_3$ grains in Series I composites. The mean particle diameter was measured at $0.96 \pm 0.49$ µm. The distribution exhibits a peak in the 1.0 to 1.2 µm range, where approximately 16% of particles fall, and most of the grains $Al_2O_3$ sizes are concentrated between 0.6 and 1.6 µm. The distribution has a narrower

spread, indicating relatively uniform grain sizes in this series.

In contrast, Figure 12 b presents the histogram illustrating the grain size distribution of $Al_2O_3$ grains in Series II composites. The mean grain diameter was measured at $1.28 \pm 0.75$ µm, which is both larger and exhibits a wider standard deviation compared to Series I. The distribution peaks in the 1.2 to 1.4 µm range, with around 16% falling in this interval. However, the grain sizes are more widely distributed, extending up to approximately 4.2 µm. This broader distribution suggests that the use of nickel (Alfa Aesar) powder, with its particle size range of 3.8 µm to 155.2 µm, contributed to increased grain growth and greater variability in particle sizes in Series II composites.

Interestingly, Series II exhibited larger average grain sizes ($1.28 \pm 0.75$ µm) compared to

Series I (0.96 ± 0.49 μm), yet still demonstrated significantly higher compressive strength. While finer grains are generally associated with enhanced strength through grain boundary strengthening, the improved mechanical performance of Series II is primarily attributed to the uniform distribution and alignment of nickel particles under the influence of the external magnetic field. This optimized microstructural arrangement reduced internal defects and enhanced interfacial bonding, allowing for more effective stress transfer and crack deflection. Thus, in this case, the quality of particle dispersion and structural integrity played a more critical role than grain size in determining compressive strength.

## CONCLUSIONS

This study demonstrates that the integration of centrifugal slip casting with an external constant magnetic field significantly enhances the microstructural uniformity and mechanical performance of $Al_2O_3$–Ni ceramic-metal composites. A direct comparison between two series fabricated using nickel powders from different suppliers (Sigma Aldrich and Alfa Aesar) revealed that the choice of powder source, and specifically the particle morphology and size distribution, plays a crucial role in determining the final properties of the composite.

The application of the magnetic field during the casting process resulted in a more uniform alignment and dispersion of nickel particles in Series II (Alfa Aesar powder), as confirmed by SEM and EDS analysis. In contrast, Series I (Sigma Aldrich powder) exhibited irregular Ni distribution and larger particle agglomeration, especially near the periphery due to centrifugal effects.

Mechanical testing showed a dramatic increase in compressive strength – from 21 MPa in Series I to 410 MPa in Series II, representing an improvement of over 1850%. This substantial gain confirms the effectiveness of particle alignment and homogeneous distribution in enhancing load-bearing capacity. Additionally, Series II samples exhibited improved ductility and more stable crack propagation, indicating a transition from predominantly intergranular fracture in Series I to more transgranular or mixed fracture modes in Series II.

These results confirm that combining centrifugal casting and magnetic field-assisted particle alignment can achieve tailored microstructures with superior mechanical properties. The study highlights the importance of raw material selection – specifically nickel particle morphology – in optimizing composite fabrication. Ultimately, the presented method provides a robust route for producing high-performance ceramic-metal composites with potential applications in aerospace, electronics, and other high-demand sectors.

## Acknowledgment

## REFERENCES

1. Ortner HM., Ettmayer P., Kolaska H. The history of the technological progress of hardmetals. International Journal of Refractory Metals and Hard Materials 2014; 44: 148–159. https://doi.org/10.1016/j.ijrmhm.2013.07.014

2. Kordani N. 9 - Materials, design, and technology of body armor, Editor(s): Shahid ul-Islam, Abhijit Majumdar, Bhupendra Butola, Textile Institute Book Series, Advances in Healthcare and Protective Textiles, Woodhead Publishing: 2023; 259–301. https://doi.org/10.1016/B978-0-323-91188-7.00006-6

3. Konopka K. Particle-reinforced ceramic matrix composites—selected examples. Journal of Composites Science 2022; 6: 178. https://doi.org/10.3390/jcs6060178

4. Rodriguez-Suarez T., Bartolome JF., Smirnov A., Lopez-Esteban S., Torrecillas R., Moya JS. Sliding wear behavior of alumina/nickel nanocomposites processed by a conventional sintering route. Journal of European Ceramic Society 2011; 31: 1389–1395.

5. Li G., Ren R., Huang X., Guo J. Microstructure and mechanical properties of $Al_2O_3$/Ni composites. Ceramic International 2004; 30: 977-982. https://doi.org/10.1016/j.ceramint.2003.11.004

6. Woźniak J. et al. $Al_2O_3$-Ni composites for cutting tools. Journal of International Scientific Publications: Materials, Methods & Technologies 2013; 7: 321–28.

7. Li G., Huang X., Guo J. Fabrication and mechanical properties of $Al_2O_3$–Ni composite from two different powder mixtures. Materials Science and Engineering: A 352 2003: 23–28. https://doi.org/10.1016/S0921-5093(02)00255-1

8. Fahrenholtz WG. Reactive hot pressing of $Al_2O_3$-Ni composites. Journal of Materials Science 2003; 38: 3073–3080. https://doi.org/10.1023/A:1024760810275

9. Hutsaylyuk V., Student M., Posuvailo V., Student O., Sirak Y., Hvozdets'kyi V., Maruschak P., Veselivska H. The properties of oxide-ceramic layers with Cu and Ni inclusions synthesizing by PEO method on top of the gas-spraying coatings on aluminium alloys. Vacuum 2020; 179: 109514. https://doi.org/10.1016/j.vacuum.2020.109514

10. Hutsaylyuk V., Student M., Posuvailo V., Student O., Hvozdets'kyi V., Maruschak P., Zakiev V. The role of hydrogen in the formation of oxide-ceramic layers on aluminum alloys during their plasma-electrolytic oxidation. Journal of Materials Research and Technology 2021; 14: 1682–1696. https://doi.org/10.1016/j.jmrt.2021.07.082

11. Cavaliere P., Sadeghi B., Shabani A. Spark Plasma Sintering: Process Fundamentals. Spark Plasma Sintering of Materials: Advances in Processing and Applications. Springer International Publishing; 2019; 3–20.

12. Laszkiewicz-Łukasik J., Putyra P., Klimczyk P., Podsiadło M., Bednarczyk K. Spark plasma sintering/field assisted sintering technique as a universal method for the synthesis, densification and bonding processes for metal, ceramic and composite materials. Journal of Applied Materials Engineering 2020; 60; 2–3. https://doi.org/10.35995/jame60020005

13. Ujah CO., Von Kallon DV., Aigbodion VS. High entropy alloys prepared by spark plasma sintering: Mechanical and thermal properties. Materials Today Sustainability 2024; 25: 100639. https://doi.org/10.1016/j.mtsust.2023.100639

14. Zhang J., Tu R., Goto T. Spark plasma sintering of $Al_2O_3$–Ni nanocomposites using Ni nanoparticles produced by rotary chemical vapour deposition. Journal of European Ceramic Society 2014; 34: 435–441. https://doi.org/10.1016/j.jeurceramsoc.2013.08.014

15. Isobe T., Daimon K., Sato T., Matsubara T., Hikichi Y., Ota T. Spark plasma sintering technique for reaction sintering of Al2O3/Ni nanocomposite and its mechanical properties. Ceramic International 2008; 34: 213–217. https://doi.org/10.1016/j.ceramint.2006.08.017

16. Kelly JP., Elmer JW., Ryerson FJ., Lee JRI., Haslam JJ. Directed energy deposition additive manufacturing of functionally graded Al-W composites. Additive Manufacturing 2021; 39: 101845. https://doi.org/10.1016/j.addma.2021.101845

17. Zhu W., Yan C., Shi Y., Wen S., Liu J., Wei Q., Shi Y. A novel method based on selective laser sintering for preparing high-performance carbon fibres/polyamide12/epoxy ternary composites. Scientific Reports 2016; 6: 33780. https://doi.org/10.1038/srep33780

18. Gómez-Rodríguez C., García-Quiñonez LV., Verdeja LF., Castillo-Rodríguez GA., Aguilar-Martínez JA., Mariño-Gámez AE., Fernández-González D. Selective laser sintering of alumina-molybdenum nanocomposites. Ceramic International 2022; 48: 29540–29545. https://doi.org/10.1016/j.ceramint.2022.08.058

19. Zygmuntowicz J., Miazga A., Wiecinska P., Kaszuwara W., Konopka K., Szafran M. Combined centrifugal-slip casting method used for preparation the Al2O3-Ni functionally graded composites. Composites Part B: Engineering 2018; 141: 158–163. https://doi.org/10.1016/j.compositesb.2017.12.056

20. Zygmuntowicz J., Wiecińska P., Miazga A. et al. $Al_2O_3$/Ni functionally graded materials (FGM) obtained by centrifugal-slip casting method. Journal of Thermal Analysis and Calorimetry 2017; 130: 123–130. https://doi.org/10.1007/s10973-017-6232-5

21. Zygmuntowicz J., Wachowski M., Miazga A., Konopka K., Kaszuwara W. Characterization of $Al_2O_3$/Ni composites manufactured via CSC technique in magnetic field. Composites Part B: Engineering 2019; 156: 113–120. https://doi.org/10.1016/j.compositesb.2018.08.079

22. Zygmuntowicz J., Kosiorek M., Piotrkiewicz P., Wachowski M., Szachogłuchowicz I., Kaszuwara W., Konopka K., Falkowski P., Piątek M. Gradient composites $Al_2O_3$-Ni obtained via the CSC technique in a magnetic field - microstructure and mechanical properties. Journal of Alloys and Compounds 2024; 1008: 176532. https://doi.org/10.1016/j.jallcom.2024.176532

23. Hidber PC., Graule TJ., Gauckler LJ. Citric acid: a dispersant for aqueous alumina suspensions. Journal of American Ceramic Society 1996; 79: 1857–1867. https://doi.org/10.1111/j.1151-2916.1996.tb08006.x

24. Gizowska M., Konopka K., Szafran M. Properties of water-based slurries for fabrication of ceramic-metal composites by slip casting method. Archives of Metallurgy and Materials 2011; 56: 1105–1110. https://doi.org/10.2478/v10172-011-0123-8

25. Hidber PC., Graule TJ., Gauckler LJ. Competitive adsorption of citric acid and poly(vinyl alcohol) onto alumina and its influence on the binder migration during drying. Journal of the American Ceramic Society 1995, 78: 1775–1780. https://doi.org/10.1111/j.1151-2916.1995.tb08888.x

26. Michalski J., Wejrzanowski T., Pielaszek R., Konopka K., Łojkowski W., Kurzydłowski KJ. Application of image analysis for characterization of powders. Mater Sci Pol 2005; 23: 79–86.

27. Kurzydlowski KJ., Ralph B. The Quantitative Description of the Microstructure of Materials, CRC Press 1995.

28. Wejrzanowski T., Spychalski W., Rożniatowski K., Kurzydłowski K. Image based analysis of complex microstructures of engineering materials.

International journal of applied and computational mathematics 2008; 18: 33–39. https://doi.org/10.2478/v10006-008-0003-1

29. Wejrzanowski T., Kurzydlowski KJ. Stereology of grains in nano-crystals. Solid State Phenomenon 2003; 94: 221–228. https://doi.org/10.4028/www.scientific.net/SSP.94.221

30. Neu V., Schultz L. Magnets: Mechanically Alloyed, Editor(s): K.H. Jürgen Buschow, Robert W. Cahn, Merton C. Flemings, Bernhard Ilschner, Edward J. Kramer, Subhash Mahajan, Patrick Veyssière, Encyclopedia of Materials: Science and Technology, Elsevier 2001, 1–4, https://doi.org/10.1016/B0-08-043152-6/00890-1

31. Crangle J., Goodman GM. The Magnetization of Pure Iron and Nickel. Proceedings of the Royal Society of London. Series A, Mathematical and Physical Sciences 1971; 321: 477–491. http://www.jstor.org/stable/77809. Accessed 12 Nov. 2024

32. Chikazumi S. Physics of Ferromagnetism. Clarendon Press 1997.

33. Jiles DC., Atherton DL. Theory of ferromagnetic hysteresis. Journal of magnetism and magnetic materials 1986; 61: 48–60. https://doi.org/10.1016/0304-8853(86)90066-1

34. Zygmuntowicz J., Kosiorek M., Wachowski M., Śnieżek L., Szachogłuchowicz I., Piotrkiewicz P., Kaszuwara W., Konopka K. The structural and mechanical properties of $Al_2O_3$–Ni composites obtained by magnetic field-assisted centrifugal slip casting. Materials 2024; 17: 3902. https://doi.org/10.3390/ma17163902